High-resolution velocity estimation from surface-based common-offset GPR reflection data

Yu Liu, James Irving*, and Klaus Holliger

Institute of Earth Sciences, University of Lausanne, CH-1015 Lausanne, Switzerland

*Corresponding author. E-mail address: james.irving@unil.ch

Summary

Surface-based common-offset ground-penetrating radar (GPR) reflection profiling is a popular geophysical exploration technique for obtaining high-resolution images of the shallow subsurface in a cost-effective manner. One drawback of this technique is that, without complementary borehole information in form of dielectric permittivity and/or porosity logs along the profile, it is currently not possible to obtain reliable estimates of the high-frequency electromagnetic velocity distribution of the probed subsurface region. This is problematic because adequate knowledge of the velocity is needed for accurate imaging and depth conversion of the data, as well as for quantifying the distribution of soil water content. To overcome this issue, we have developed a novel methodology for estimating the detailed subsurface velocity structure from common-offset GPR reflection measurements, which does not require additional conditioning information. The proposed approach combines two key components: Diffraction analysis is used to infer the smooth, large-scale component of the velocity distribution, whereas the superimposed small-scale fluctuations are inferred via inversion of the reflected wavefield. We test and validate our method on two synthetic datasets having increasing degrees of complexity and realism before applying it to a field example from the Boise Hydrogeophysical Research Site (BHRS), where independent control data in the form of neutron-neutron porosity logs are available for validation. The results obtained demonstrate the viability and robustness of the proposed approach. Further, due to its efficiency, both in terms of field effort and computational cost, the method can be readily extended to 3D, which further enhances its attractiveness compared to multi-offset-based GPR velocity estimation techniques.

Abbreviated title: Velocity estimation from common-offset GPR data

Keywords: Electrical properties; Hydrogeophysics; Electromagnetic theory; Ground penetrating radar; Inverse theory; Wave scattering and diffraction.

1 Introduction

Ground-penetrating radar (GPR) is a high-resolution geophysical exploration technique that has the potential of providing images of shallow subsurface structure with a resolution in the meter to decimeter range (e.g., Knight 2001; Annan 2005; Klotzsche et al. 2018; Lai et al., 2018). Whereas borehole-based GPR transmission techniques have proven to be well-suited to full-waveform inversion approaches (e.g., Ernst et al. 2007; Klotzsche et al. 2019), estimating the detailed velocity structure of the subsurface from surface-based GPR reflection data is notoriously difficult. This is problematic because: (i) the overwhelming majority of GPR data are acquired in reflection mode along the Earth's surface; (ii) accurate velocity information is necessary for proper imaging of reflection data; and (iii) the high-frequency electromagnetic wave velocity in the GPR regime has a strong and direct sensitivity to soil water content, which is a key parameter for many hydrogeological, agricultural, and engineering applications (e.g., Huisman et al. 2003).

One common approach for subsurface velocity estimation from reflection GPR measurements is to collect data at multiple transmitter-receiver offsets and to perform either normal-moveout (NMO) velocity analysis (e.g., Greaves et al. 1996; Huisman et al. 2003; Perroud & Tygel 2005) or reflection tomography (e.g., Bradford 2008). With regard to NMO, the inherent assumption of 1D horizontal layering means that it cannot effectively deal with the highly heterogeneous velocity structures that are rather common in near-surface investigations. Although reflection tomography is able to overcome this issue, it comes at a rather high computational cost and requires inherently subjective horizon picking. Further, as pointed out by Bradford et al. (2009), reflection tomography only recovers the large-scale component of the subsurface velocity distribution that is needed to properly focus and image the GPR data, which is of substantially lower resolution than the reflection image itself. The latter problem can be potentially alleviated through waveform inversion approaches (e.g., Busch et al. 2012; Lavoué et al. 2014); however their success so far has been limited due to the rather narrow range of reflection angles and antenna radiation patterns that are highly complex, largely unknown, and site-dependent (e.g., Lampe & Holliger 2003). Finally, a clear drawback of multi-offset GPR acquisitions is their high cost in terms of acquisition time, which increases approximately linearly with the considered number of transmitter-receiver offsets for the common case of GPR systems having a single transmitter and receiver antenna. Indeed, such surveys become largely impractical in the context of long 2D profiles and, particularly, 3D acquisitions.

For the above reasons, the vast majority of surface-based GPR reflection surveys are performed using the traditional bi-static, common-offset approach, where a single transmitter-receiver antenna pair, separated by a small fixed distance, is incrementally moved along the measurement profile (e.g., Annan 2005). While the estimation of the subsurface velocity distribution from such data is substantially more difficult than for multi-offset GPR surveys, significant efforts have been made during the past decade because of the high potential rewards. In this regard, Schmelzbach et al. (2012) present an impedance inversion approach for common-offset GPR data that is based on a convolution model for the GPR traces, where borehole dielectric permittivity or porosity logs are used to recover the low-frequency part of the velocity structure that cannot be obtained from the reflection data. Zeng et al. (2015) and Liu et al. (2018) adopt similar approaches to estimate the distribution of soil water content and to characterize buried archaeological remains, respectively. Xu et al. (2021) also assume a convolution model for the GPR traces, but combine stochastic simulation with simulated annealing optimization in order to generate velocity realizations that honor the GPR measurements and borehole porosity log data along the profile. Forte et al. (2013; 2014) assume a locally 1D layered subsurface structure and use picked reflection amplitudes to recursively estimate the GPR velocity in a series of identified subsurface layers, in which the velocity is assumed constant. Other authors estimate the spatial distribution of GPR velocity from common-offset data via the analysis of diffractions present in the recordings. Novais et al.

(2008) use velocity continuation to generate several migrated sections and analyze the associated diffraction focusing to build a root-mean-square (RMS) velocity model. Clair & Holbrook (2017) apply the seismic diffraction imaging and velocity analysis workflow proposed by Fomel et al. (2007) to common-offset GPR data in order to estimate snow water equivalent. Yuan et al. (2019) employ a similar approach to characterize the velocity structure of surficial chalk deposits. Although all of the above methods have the ability to estimate subsurface properties from common-offset GPR measurements, they all suffer from inherent limitations. Notably, the reflection-based methods have the potential to provide high-resolution results, but they generally require complementary information such as borehole logs, which are usually not available. Conversely, diffraction-based methods require a suitably dense and even distribution of diffractions in the data and, even under ideal circumstances, can only resolve the large-scale velocity structure.

In this study, we present a novel velocity estimation method for surface-based common-offset GPR reflection data that combines the advantages of the reflection- and diffraction-based techniques described above. To estimate the low-frequency background velocity field, diffractions are separated from the unmigrated GPR data and subjected to migration velocity analysis based on a prescribed focusing measure. After migrating the GPR data using the derived velocity field, the reflected wavefield is isolated and used to deduce the small-scale velocity fluctuations. The latter is accomplished via sparse inversion based on an iteratively reweighted least-squares strategy assuming a convolutional model for each GPR trace. The final high-resolution velocity distribution is obtained by combining the large-scale diffraction-based and the fine-scale reflection-based estimates.

The paper proceeds as follows. We begin by describing the methodological background of the proposed velocity estimation method. Next, we show the application of our method to two synthetic datasets, which differ in their degree of complexity and realism. Finally, we apply the proposed approach to common-offset 100-MHz GPR field data acquired at the Boise Hydrogeophysical Research Site (BHRS) near Boise, Idaho, USA.

2 Methodology

We assume in our work that the subsurface velocity distribution $v(x,z)$ can be regarded as the sum of a smoothly varying or constant background velocity field $v_0(x,z)$ and a small-scale velocity fluctuation field $\Delta v(x,z)$ (e.g., Pullammanappallil et al. 1997; Poppeliers 2007; Irving et al. 2009; Scholer et al. 2010)

$$v(x,z) = v_0(x,z) + \Delta v(x,z). \tag{1}$$

To determine $v(x,z)$ from a common-offset GPR reflection dataset, we separate the recorded wavefield into its diffracted and reflected components, which are used to estimate v_0 and Δv, respectively. This inherently assumes that the background velocity field is smooth at the scale of a dominant GPR wavelength and beyond, such that it does not contribute to the reflected wavefield. Figure 1 illustrates schematically the steps involved in our velocity estimation procedure. First, diffractions are separated and analyzed in order to infer the spatially variable RMS and interval velocity structures. The latter serves as v_0, whereas the former is used to migrate the common-offset GPR data, after which the dominant reflections are separated.

Assuming a convolutional relationship between the velocity perturbation field and the reflection data based on an estimated mixed-phase wavelet, a L1-norm constrained inversion is then used to infer Δv. Below we describe in detail this inversion workflow in terms of the following four main components: (i) diffraction separation, (ii) background velocity estimation, (iii) reflected wavefield prediction, and (iv) velocity perturbation inversion.

2.1 Diffraction separation

The diffracted wavefield is obtained in our methodology via plane-wave destruction (PWD) filtering (Fomel, 2002). The underlying assumption when using this approach is that reflections correspond primarily to coherent events having slowly changing slopes in the *x*-*t* domain, whereas the slopes associated with diffractions are significantly more spatially variable. The goal of PWD filtering is to destroy locally planar events in the data corresponding to an estimated slope field $\sigma(x,t)$. By regularizing the estimation problem, it is possible to destroy only those events whose slopes change slowly in space, thereby isolating the diffracted energy.

A local plane wave in the *x*-*t* domain can be expressed by the following differential equation (e.g., Fomel, 2002):

$$\frac{\partial u}{\partial x}+\sigma\frac{\partial u}{\partial t}=0, \tag{2}$$

where $u(x,t)$ is the wavefield and σ is the local slope. If the local slope in a seismic or GPR dataset is unchanging in time, the wavefields observed at two adjacent trace positions x_i and x_{i+1} are related by a time shift $\sigma\Delta x$, where Δx is the trace spacing. That is,

$$u(x_{i+1}, t) = u(x_i, t + \sigma \Delta x), \tag{3}$$

which has the Fourier transform

$$U(x_{i+1}, \omega) = U(x_i, \omega) e^{i\omega\sigma\Delta x}. \tag{4}$$

Equation (4) shows that we can predict the trace at position x_{i+1} from the trace at position x_i by application of a linear phase shift. To apply this concept to data with temporally variable local slopes, Fomel (2002) used the fractional delay filter of Thiran (1971) to derive a localized, discrete, time-domain approximation to $e^{i\omega\sigma\Delta x}$ whose coefficients depend nonlinearly on the local slope values. Prediction of a trace using its neighbor can then be accomplished by matrix-vector multiplication

$$\mathbf{u}_{i+1} = \mathbf{P}_{i,i+1}\mathbf{u}_i, \tag{5}$$

where $\mathbf{P}_{i,i+1}$ is a time-variable convolution matrix linking trace vectors $\mathbf{u}_{i+1}$ and $\mathbf{u}_i$, whose entries are a nonlinear function of the local slope field $\sigma(x, t)$.

The PWD problem seeks to estimate $\sigma(x, t)$ by minimizing the prediction error for an entire seismic or GPR section, thereby destroying the local plane waves in the data. Considering the section $\mathbf{s}$ as a column vector containing all of the traces, i.e., $\mathbf{s} = [\mathbf{s}_1^{\mathrm{T}}\ \mathbf{s}_2^{\mathrm{T}} \ldots \mathbf{s}_{\mathrm{n}}^{\mathrm{T}}]^{\mathrm{T}}$, this is described by

$$\mathbf{r} = \mathbf{D}\mathbf{s}, \tag{6}$$

where $\mathbf{r}$ is the destruction residual, and $\mathbf{D}$ is the destructor matrix defined by:

$$\mathbf{D} = \begin{bmatrix} -\mathbf{P}_{1,2} & \mathbf{I} & 0 & \cdots & 0 \\ 0 & -\mathbf{P}_{2,3} & \mathbf{I} & \cdots & 0 \\ \cdots & \cdots & \cdots & \cdots & \cdots \\ 0 & \cdots & 0 & -\mathbf{P}_{\mathrm{n-1,n}} & \mathbf{I} \end{bmatrix}, \tag{7}$$

with $\mathbf{I}$ representing identity operator. The estimation of $\sigma(x, t)$ is accomplished via regularized nonlinear least-squares minimization of equation (6), where shaping regularization (Fomel 2007a) is used to control the smoothness of the estimated slope field. In our case, the considered lateral smoothing radius for the regularization must be large enough to estimate a slope field that well represents the reflections in the dataset, but not the diffractions. The prediction residual corresponding to the estimated slope field is simply the GPR section with the reflection events removed. All of the above steps are performed in our work using the programs 'sfdip' and 'sfpwd' in Madagascar (https://reproducibility.org/), an open-source data analysis package.

2.2 Background velocity estimation

Once the diffracted wavefield has been separated, the next step is to use it to estimate the low-frequency background velocity field v_0, which, due to its smoothness at the wavelength scale, does not to contribute to the reflected wavefield. To this end, we first estimate the RMS velocity distribution by examining the focusing of diffractions during migration using a suite of constant velocity values. Fomel et al. (2007) proposed a migration focusing metric based on local kurtosis, whereas Decker et al. (2017) considered the local semblance attribute. Here, we use the latter measure, which can be defined as

$$s(x,t,v) = \frac{\left(F_v\big(a(x,t)\big)\right)^2}{F_v\big(\, a^2(x,t)\big)}, \tag{8}$$

where $a(x,t)$ denotes the diffraction amplitude as a function of horizontal position x and time t, and operator F_v denotes time migration using constant velocity v. Migration is performed on both the diffracted wavefield and its square using the velocity continuation method of Fomel (2003), which results in two space-time-velocity cubes. In Madagascar, this step is accomplished using the program ‘sfvelcon’. The division in equation (8) is then performed in a regularized manner using the program 'sfdivn' in order to constrain the smoothness of the resulting local semblance cube (Fomel, 2007b). Using the automatic picking algorithm 'sfpick' (Fomel, 2009), the maxima on each time-velocity panel are next selected, which yields a 1D RMS velocity curve at each trace location. These curves are combined into a 2D RMS velocity model, which is finally provided as input to the constrained Dix inversion program 'sfdix' (Fomel and Guitton, 2006) to estimate $v_0(x, t)$.

2.3 Reflection separation

In order to obtain the reflected wavefield that is used in our inversion procedure to estimate the velocity perturbation Δv, two steps are performed. First, the GPR profile is time-migrated based on the inferred RMS velocity model from Section 2.2 using the velocity continuation method described in Fomel (2003). This has the effect of collapsing diffractions and moving dipping reflectors to their correct positions in terms of vertical traveltime, and is accomplished using the Madagascar programs 'sfvelcon' and 'sfslice'. Then, we apply the PWD method to the migrated reflection section in order to estimate the local slopes, which in this case are used to predict the time-migrated reflected wavefield void of migration artifacts and random noise (Fomel and Guitton, 2006). The latter step is accomplished using the Madagascar program ‘sfpwdsmooth2’. Note that our use of PWD here is different compared to what was presented in Section 2.1, where the method was used to suppress reflected energy in the data and isolate the diffracted wavefield. In this regard, it is important to note that a high-quality reflection section cannot be obtained by simply subtracting the diffracted wavefield from the GPR data. Indeed, predicting the reflected wavefield from the estimated slopes of the time-migrated image results in a cleaner section that is much more amenable to the velocity perturbation inversion described next.

2.4 Velocity perturbation inversion

To estimate the velocity perturbation field Δv, we perform sparse inversion of the time-migrated reflected GPR wavefield obtained in Section 2.3. To this end, we assume that the wavefield can be effectively described using the so-called primary reflectivity section (PRS) model (e.g., Gibson and Levander, 1990; Holliger et al., 1994; Irving et al., 2009), whereby the time-migrated data, $d(x,t)$, are expressed as the convolution product of the GPR source wavelet, $\mathrm{w}(t)$, and the subsurface reflectivity distribution, $r(x,t)$

$$d(x,t) = \mathrm{w}(t) * r(x,t). \tag{9}$$

Equation (9) is well known to provide an adequate model for zero-offset seismic or GPR reflection data when single scattering prevails and dispersion is absent (e.g., Yilmaz, 2001). P Although the second assumption is only strictly valid for GPR data acquired in perfectly electrically resistive environments, experience has shown that this model is able to accommodate the limited dispersion effects linked to low-loss conditions for which the GPR method is suitable (e.g., Irving et al., 2009; Xu et al., 2020). Indeed, such effects in GPR data tend to be inherently rather minor, as it is simply impossible to acquire high-quality GPR reflection data in strongly dispersive environments.

As the subsurface reflectivity can be approximated using the temporal derivative of the velocity perturbation field (e.g., Pullammanappallil et al. 1997; Poppeliers 2007), and because the temporal derivative operator may be treated as a finite-difference filter whose position within a convolution equation can be shifted (Irving et al. 2009; Scholer et al. 2010), equation (9) leads to

$$\begin{aligned} d(x,t) &\approx \mathrm{w}(t) * \frac{\partial}{\partial t}\Delta v(x,t) \\ &= g(t) * \Delta v(x,t), \end{aligned} \tag{10}$$

where $g(t)$ represents the time-differentiated GPR wavelet. Expression (10) provides a linear relationship between the time-migrated reflected GPR wavefield and the velocity perturbation field, which forms the basis for our inversion procedure. Indeed, considering data vector $\mathbf{d}$ containing all of the GPR traces arranged into a single column, i.e., $\mathbf{d} = [\mathbf{d}_1^{\mathrm{T}}\ \mathbf{d}_2^{\mathrm{T}}\ \ldots\ \mathbf{d}_{\mathrm{n}}^{\mathrm{T}}]^{\mathrm{T}}$, and model vector $\mathbf{m}$ containing the corresponding velocity perturbations underlying each trace arranged into a single column, i.e., $\mathbf{m} = [\boldsymbol{\Delta}\mathbf{v}_1^{\mathrm{T}}\ \boldsymbol{\Delta}\mathbf{v}_2^{\mathrm{T}}\ \boldsymbol{\Delta}\mathbf{v}_3^{\mathrm{T}}\ \ldots\ \boldsymbol{\Delta}\mathbf{v}_{\mathrm{n}}^{\mathrm{T}}]^{\mathrm{T}}$, we have

$$\mathbf{d} = \mathbf{G}\mathbf{m}, \tag{11}$$

where $\mathbf{G}$ is a block-diagonal matrix containing n replicates of the convolution matrix associated with the time-differentiated wavelet $g(t)$.

To define the kernel matrix **G**, information on the GPR source wavelet is required. In this work, we estimate $w(t)$ from the reflected wavefield using the method of Schmelzbach & Huber (2015), which assumes that a typical mixed-phase GPR source wavelet can be considered as a minimum-phase wavelet that has been shifted by a constant phase angle. To first estimate the corresponding minimum-phase wavelet, we perform standard least-squares spiking deconvolution on the reflected wavefield and take the inverse of the deconvolution operator (e.g., Buttkus, 2000). A search of the phase rotation angle that maximizes the kurtosis when applied to this minimum-phase wavelet is then used to obtain the final mixed-phase GPR source wavelet. The practical validity of this source wavelet estimation procedure was recently demonstrated by Xu et al. (2021). Note that the effects of minor dispersion in the GPR data are, at least in part, accounted for in the sense that an effective wavelet that best fits the considered dataset in its entirety, rather than the true emitted GPR source signal, is estimated.

To invert for the velocity perturbation $\mathbf{m}$ given the reflection data $\mathbf{d}$, we minimize the following objective function

$$\theta(\mathbf{m}) = ||\mathbf{Gm} - \mathbf{d}||_2^2 + \lambda \, \|\mathbf{Dm}\|_1, \tag{12}$$

where $\|\cdot\|_p$ denotes the L-p norm, λ is a trade-off parameter that controls the desired balance between fitting the data and honoring the prescribed prior information about the model, and matrix $\mathbf{D}$ is given by

$$\mathbf{D} = \begin{bmatrix} \mathbf{D}_\mathrm{x} \\ \alpha \, \mathbf{D}_\mathrm{t} \end{bmatrix}. \tag{13}$$

Here, $\mathbf{D}_\mathrm{x}$ and $\mathbf{D}_\mathrm{t}$ are finite-difference matrices that approximate the first derivatives of the velocity perturbation model in the horizontal and temporal directions, respectively, and α is an anisotropy parameter that controls the degree of desired smoothing between the temporal and horizontal directions. The choice of α should reflect the expected aspect ratio of the underlying GPR velocity heterogeneity.

Equation (12) corresponds to a regularized least-squares inversion with blocky model prior constraints. That is, in seeking to minimize the L1-norm of the first derivatives of the velocity perturbation field, we tend to recover models that have a sparse first derivative structure, meaning a piecewise-constant or blocky appearance. Note that this approach has similarities to sparse spike deconvolution in seismic data processing, which uses sparsity constraints to recover the underlying reflectivity series from a seismic trace (e.g., Claerbout and Miur, 1973; Oldenburg et al., 1983; Velis, 2008). Our method differs, however, in the sense that (i) we use sparsity applied to the first derivative of the velocity perturbation field and invert for the latter directly, rather than inverting for a sparse reflectivity series; and (ii) we invert all traces at once with both vertical and lateral regularization constraints in order to estimate the full 2D velocity perturbation field.

Due to the presence of the L1-norm, the minimization of equation (12) is nonlinear. To address this, we use an iteratively reweighted least squares (IRLS) approach based on the following approximation of the Lp-norm proposed by Ekblom (1973):

$$\|\mathbf{x}\|_p \approx \sum_{i=1}^{n} (x_i^2 + \epsilon^2)^{p/2}, \tag{14}$$

where ϵ is a small user-defined value (e.g., Farquharson and Oldenburg, 1998). Taking the derivative of equation (12) with respect to $\mathbf{m}$ and setting it to zero, and considering approximation (14), we arrive at

$$(2\mathbf{G}^{\mathbf{T}}\mathbf{G} + \lambda \mathbf{D}^{T}\mathbf{R}\mathbf{D})\,\mathbf{m} = 2\mathbf{G}^{\mathbf{T}}\mathbf{d}, \tag{15}$$

where

$$\mathbf{R}_{ii} = \frac{1}{|(\mathbf{Dm})_i| + \epsilon} \tag{16}$$

is a diagonal reweighting matrix. We solve for $\mathbf{m}$ iteratively as follows:

(1) Set $\mathbf{R} = 2\mathbf{I}$.

(2) Solve equation (15) for $\mathbf{m}$ using the conjugate gradient method.

(3) Update $\mathbf{R}$ using equation (16) and the result for $\mathbf{m}$ obtained in Step 2.

(4) Return to Step (2) and iteratively update $\mathbf{m}$ until a defined maximum number of iterations or desired data fit is reached.

In carrying out the above steps, the first iteration of our inversion procedure solves for the velocity perturbation field corresponding to an L2-norm constraint on the model derivative term in equation (12). This and subsequent solutions are then used within the IRLS reweighting scheme in order to gradually converge to the L1-norm solution, typically within a few iterations. Once $\Delta v(x,t)$ has been obtained, it is added to the estimated background velocity model $v_0(x,t)$ from Section 2.2. As a final step, the resulting subsurface velocity field in terms of vertical two-way traveltime, $v(x,t)$, is converted to depth to obtain the desired $v(x,z)$.

3 Results

3.1 Application to synthetic data

In the following, we test and validate the velocity estimation technique outlined in Section 2 and illustrated in Figure 1 by applying it to synthetic common-offset GPR reflection data. We first consider a layered subsurface velocity model containing a small number of well-defined point-type diffractors. We then move to an arguably more realistic scenario involving a stochastic velocity distribution characterized by the explicit absence of idealized diffracting structures.

3.1.1 Layered model

Our layered velocity model, which is shown in Figure 2a, is similar to that recently considered by Yuan et al. (2019) in a diffraction imaging study. The model contains two main velocity units separated by a dipping interface. A thin horizontal bed, with a thickness of 0.5 m, is present in the underlying unit. Both the upper and lower units contain three circular diffractors with diameters ranging from 0.4 to 0.6 m. The corresponding relative dielectric permittivities of the upper and lower layers, the thin bed, and the diffractors are 9, 16, 25, and 4, respectively. The electrical conductivity of all materials is fixed at a constant value of 1 mS/m, and the magnetic permeability is assumed to be equal to its value in free space.

Synthetic common-offset GPR reflection data were simulated over the layered velocity model using the gprMax software (Warren et al. 2016), which solves Maxwell's equations using the finite-difference time-domain (FDTD) method. The transmitter and receiver antennas, which are approximated by point electric dipoles, were spaced 0.5 m apart and moved at 0.1 m increments along the survey profile. The source antenna current function was specified as a Ricker wavelet having a dominant frequency of 100 MHz, which resulted in a propagating electromagnetic pulse corresponding to the first derivative of this function. The resulting synthetic GPR data were then contaminated with 2% Gaussian random noise (Figure 2b) prior to being subjected to a standard processing flow involving (i) elimination of the direct air and ground arrivals from the data by subtracting the average trace calculated over a time window from 0 to 36 ns using a moving spatial window of 50 traces; (ii) amplitude scaling to compensate for energy spreading, absorption, and scattering using a gain function of the form $g(t) = (1 + at)e^{bt}$; and (iii) 5-300 Hz bandpass filtering. With time measured in nanoseconds, the parameters a and b were chosen empirically to be 0.3 ns^{-1} and 0.2 ns^{-1}, respectively, such that the gain function brought all amplitudes along a given trace to the same average level. Figure 3a shows the resulting unmigrated processed data section.

Following the velocity estimation workflow outlined in Section 2 and illustrated in Figure 1, diffractions were first separated from the processed data using PWD filtering (Figure 3b). The diffracted wavefield was then subjected to velocity continuation and local kurtosis analysis in order to estimate the RMS velocity structure (Figure 3c), which was used in a Dix inversion procedure to obtain the low-frequency background velocity field diplayed in Figure 3d. Note that this result shows some resemblance to the underlying model in Figure 2a. However, it fails to adequately represent the dipping interface as a sharp discontinuity having a constant slope, and it entirely misses the thin bed. In Figure 3e, we show the GPR reflection data after time migration based on the estimated RMS velocity structure in Figure 3c. We see that the data have been adequately imaged apart from some residual “smiles”, which are attenuated through the application of PWD to isolate the specular reflections (Figure 3f). From the separated reflection image, a mixed-phase GPR wavelet was estimated (Schmelzbach & Huber 2015), which is compared with the first derivative of the Ricker source current function in Figure 3g. Figure 3h shows the velocity perturbation field inferred through our L1-norm inversion approach using a value of $\alpha = 10$ and after 5 IRLS iterations. We observe that the high-frequency elements present in Figure 2a have now been estimated, but not the low-frequency velocity trend. Finally, Figures 3i and 3j show the complete estimated velocity model, equal to the sum of the background and perturbation fields, in terms of two-way traveltime and after conversion to depth, respectively. The comparison with the reference velocity model (Figure 2a) is quite favorable, which clearly illustrates the potential benefits of the proposed diffraction- and reflection-based velocity estimation approach. In this context, is important to emphasize that the former can only resolve the smooth large-scale velocity structure and, hence, entirely misses the presence of the thin bed (e.g., Yuan et al. 2019) whereas, on its own, the latter requires coincident borehole information for calibration and recovery of the large-scale component of the velocity structure (e.g., Schmelzbach et al. 2012; Xu et al. 2021).

3.1.2 Heterogeneous model

We now test our proposed methodology on an arguably more realistic model of the shallow subsurface. In this regard, we consider the stochastic velocity distribution shown in Figure 4a, which is meant to emulate a heterogeneous surficial alluvial environment. The model was geostatistically generated based on the von Kármán autocorrelation function, which describes a band-limited fractal medium (e.g., Tronicke & Holliger 2005) and is given by

$$C(r) = \frac{r^{\nu} K_{\nu}(r)}{2^{\nu-1}\Gamma(\nu)}, \tag{17}$$

where $K_{\nu}(r)$ is the modified Bessel function of the second kind of order $0 \leq \nu \leq 1$, Γ is the gamma function and

$$r = \sqrt{(x/a_x)^2 + (z/a_z)^2} \tag{18}$$

is the weighted radial autocorrelation lag with a_x and a_z denoting the correlation lengths along horizontal and vertical directions x and z, respectively. Values of $\nu = 0.5$, $a_x = 2.0$ m, and $a_z = 0.2$ m were considered, along with a mean velocity of 0.1 m/ns and a standard deviation equal to 0.01 m/ns. The generated multi-Gaussian velocity realization was then transformed into a facies-type distribution through thresholding, whereby six units having constant velocities equal to 0.079, 0.092, 0.100, 0.105, 0108, and 0.116 m/ns were specified.

To generate synthetic common-offset GPR reflection data over the velocity model in Figure 4a, we again used the gprMax software (Warren et al. 2016). Velocity values v were converted to relative dielectric permittivity ε for the FDTD modeling using the low-loss approximation $v \approx 1/\sqrt{\varepsilon\mu}$, where the magnetic permeability μ was assumed equal to its value in free space. As was done previously, the electrical conductivity was fixed at a constant value of 1 mS/m. For the source antenna current function, we considered for this simulation the derivative of a Blackman-Harris window having a dominant frequency of 100 MHz (Irving and Knight, 2006). The spacing between the transmitter receiver antennas was again set to 0.5 m, and traces were simulated every 0.1 m along the profile. Figure 4b shows the resulting synthetic GPR data with the addition of 2% Gaussian noise. Processing of these data was essentially identical to that for the layered synthetic velocity model except that the averaging window used for the first-arrival removal was set from 0 to 25 ns, and the gain parameters a and b were set to 0.2 ns^{-1} and 0.2 ns^{-1}, respectively. The processed GPR section is shown in Figure 5a.

Figure 5b shows the diffracted wavefield estimated from the processed data in Figure 5a, which was used to infer the RMS velocity structure (Figure 5c) and, subsequently, the background velocity field through Dix inversion (Figure 5d). In Figure 5e, we show the time-migrated GPR section based on the RMS velocity field, from which the reflected wavefield was obtained (Figure 5f). The latter was used to estimate an effective mixed-phase source wavelet, which is shown in Figure 5g and seen to compare favorably to the true source wavelet corresponding to the derivative of the considered input current function. Finally, in Figures 5h, 5i, and 5j, we show the inverted velocity perturbation field obtained after 5 IRLS iterations using a value of $\alpha = 10$, along with the final estimated velocity model in terms of two-way traveltime and depth, respectively. Comparison of Figure 5j with the underlying velocity model in Figure 4a demonstrates remarkably good agreement, but also points to two interesting aspects of the proposed velocity estimation method that did not become evident in its application to the more idealized layered model (Figures 2 and 3). The first concerns the influence of the direct wave and its muting, which, in the presence of small-scale heterogeneity, inherently affects the viability and accuracy of the velocity estimation over a depth range corresponding to approximately one dominant wavelength, that is, the first ~1 m depth. The second observation concerns the importance of the background velocity model and its impact on the final result. This is illustrated by the fact that our final velocity model (Figure 5j) misses the pervasive low-velocity zone between ~2 and ~3.5 m depth in the central and right-hand side of the model from ~7 m to ~20 m lateral distance, which can be directly related to the limited resolution of the estimated background velocity model.

3.2 Application to field data

3.2.1 Database

We now apply the proposed velocity estimation method to a field GPR dataset acquired at the Boise Hydrogeophysical Research Site (BHRS). The BHRS is a research wellfield located on a gravel bar adjacent to the Boise River near Boise, Idaho, USA (Figure 6). The surficial aquifer consists of late Quaternary fluvial deposits dominated by gravel and sand, and is underlain by a layer of red clay at ~20 m depth (Barrash & Clemo 2002). The depth of the groundwater table at the site varies seasonally between ~2 m and ~4 m. Over the past two decades, the BHRS has been extensively utilized for the testing, validation, and improvement of a wide variety of geophysical and hydrogeological characterization methods (e.g., Tronicke et al. 2004; Bradford et al. 2009; Dafflon et al. 2009, 2011; Hochstetler et al. 2016; Xu et al. 2020, 2021).

The considered common-offset, bi-static GPR reflection prosfile is a part of 3D survey performed at the BHRS in 1998 using a Pulse Ekko Pro 100 system (Sensors & Software Inc.) with 100 MHz nominal center frequency antennas, and can be considered as a reference for surface-based GPR reflection data collected in alluvial environments (e.g., Xu et al., 2020, 2021). The profile has a length of 30 m and crosses three boreholes, B5, A1, and B2, for which neutron-neutron porosity logs are available below the groundwater table (Figure 6). While the exact values have not been reported, the depth of the latter at the time of acquisition of the GPR data and neutron-neutron logs was approximately 2 m. The GPR data were collected using a constant antenna spacing of 1 m, a lateral trace increment of 0.1 m, and a time sampling interval of 0.8 ns. For each recorded trace, 32 stacks were performed to improve the signal-to-noise ratio. Antenna positioning errors and differences in antenna coupling across the profile were estimated to be negligible. Figure 7 shows the GPR reflection section after minor pre-processing.

3.2.2 Velocity estimation

The considered field GPR data were subjected to a processing flow consisting of, in order, time-zero correction, DC shift removal, "de-wow" filtering, removal of the direct air and ground arrivals, correction for the antenna offset, and amplitude scaling. Time-zero was determined based on the first deflection of the data above the ambient noise level. While slightly different approaches are possible, we estimate that the corresponding uncertainties do not exceed ~2 ns. To correct for antenna offset, we used the average velocity of the vadose zone of 0.14 m/ns inferred from previous work (e.g., Bradford, 2008; Bradford et al., 2009). Contrary to our synthetic examples which involved an antenna spacing of 0.5 m, correction for the larger offset between the antennas in the case of the BHRS data was deemed necessary and should lead to negligible differences in traveltime beneath the direct air and ground arrivals compared to the corresponding zero-offset acquisition. Due to the proximity of the direct arrivals to the reflection from the groundwater table, we used a manual surgical mute to remove them as opposed to the average trace subtraction technique considered previously. As was done for the synthetic data, amplitude scaling was performed using a gain function of the form $g(t) = (1 + at)e^{bt}$, where the parameters a and b that best balanced the amplitudes along any given trace were found to be 0.5 ns^{-1} and 0.8 ns^{-1}, respectively. It is important to emphasize that, with this choice of gain function that smoothly varies in time, the relative reflection amplitudes along the GPR traces are importantly well preserved, which would not be the case with the use of an AGC-type amplitude scaling.

Figure 8a shows the processed GPR section, to which we then applied the proposed velocity estimation methodology. Following the workflow described in Section 2 and illustrated in Figure 1, we began with the separation of the diffractions (Figure 8b) which, although not evident in the original processed data, turn out to be quite abundant, particularly in the central part of the profile. This was followed by the estimation of the RMS velocity structure (Figure 8c) and subsequent Dix inversion to infer the background velocity field (Figure 8d). The latter points to the presence of a rather prominent low-velocity zone at intermediate depths in the left-hand side of the profile. The inferred RMS velocity structure was then used to perform time-migration of the GPR section (Figure 8e) which, overall, appears to result in an adequate focusing and imaging of the data. An exception are the artefacts introduced into the uppermost part of the section, which are likely related to the harsh surgical muting of the direct wave as well as its potential interference with the neighboring reflection from the groundwater table. Figure 8f shows the reflected wavefield that was extracted from the migrated section, which we see to be largely devoid of these artefacts. After estimating the effective mixed-phase source wavelet (Figure 8g) using the method of Schmelzbach and Huber (2015), we proceeded to invert the imaged reflected wavefield for the underlying velocity perturbations using a value of $\alpha = 10$, whose choice was based on the typical aspect ratio encountered in similar heterogeneous environments as well as previous BHRS studies (Gelhar, 1993; Xu et al., 2020, 2021). The results, which are shown in Figure 8h, clearly depict the dramatic velocity discontinuity associated with the groundwater table. Finally, Figures 8i and 8j show the superposition of the large-scale background velocity structure (Figure 8d) and the inverted small-scale velocity perturbation field (Figure 8h) in terms of two-way traveltime and depth, respectively. Note that in deriving the latter, we also accounted for some mild topographic variations that were present along the profile. Note that, in the case fo significant topographic variations, such variations would need to be corrected for earlier in our analysis procedure.

Although the inferred velocity distribution presented in Figure 8j is clearly dominated by the sharp transition from high to low velocities across the water table, the underlying saturated zone shows a significant degree of velocity heterogeneity. This heterogeneity largely emulates the structure depicted by the reflected wavefield in Figure 8d and, as such, is geologically plausible. To further assess the realism of our results, we compare them with the neutron-neutron porosity logs available in the saturated zone for boreholes B5, A1, and B2 (Figure 6). To this end, we transform the porosity logs to GPR velocity v using a standard petrophysical mixing model (e.g., Huisman et al. 2003)

$$v = \frac{c}{\sqrt{\varepsilon_r^s}(1-\phi) + \sqrt{\varepsilon_r^w}\phi}, \tag{19}$$

where $c =$ 0.3 m/ns is the speed of light in free space, ϕ is the porosity, and $\varepsilon_r^s = 4.6$ and $\varepsilon_r^w = 80$ are the relative dielectric permittivities of the dry solid matrix and water, respectively. A relative dielectric permittivity of 4.6 for the dry matrix corresponds to the average value for quartz (e.g., Schön, 2015) and, as such, is widely regarded as being suitable for alluvial environments in general and the BHRS in particular. Indeed, Dafflon et al. (2009) demonstrated the overall suitability of a relative dielectric permittivity of 4.6 for the solid matrix at the BHRS.

While variations in this parameter on the order of 10 to 15% are conceivable, the associated uncertainties are minor and, hence, largely irrelevant compared to other sources of uncertainty in our inversion results and the neutron-neutron logs.

Figure 9 shows the comparison between the GPR-derived velocity and the converted porosity logs at the borehole locations. Overall, we see that the curves are in good agreement, not only in terms of the trend, but also with regard to the absolute values. In this context, it is important to note that the inferred velocity estimates are at least as accurate as those previously inferred from multi-offset GPR reflection tomography (Bradford et al., 2009), while at the same time exhibiting a significantly higher resolution. Arguably, the most conspicuous mismatch between the GPR- and neutron-neutron-based velocity profiles is a seemingly systematic depth shift of ~+0.5 m of the former with regard to the latter, which was recently discussed by Xu et al. (2021). This could be related to the depth calibration of the neutron-neutron logs and/or to a systematic overestimation of the GPR velocity in the vadose zone, the latter of which is the most poorly constrained part of our inferred velocity model due to partial interference between the direct arrivals and the reflection from the water table. Conversely, this apparent mismatch is unlikely to be related to the time-zero determination, whose uncertainty is estimated to be on the order of 2 ns.

4 Discussion and Conclusions

We have presented in this paper a novel method for estimating the detailed high-frequency electromagnetic velocity distribution in the shallow subsurface from surface-based common-offset GPR reflection data. The smooth background component of the velocity structure is estimated from the diffracted part of the recorded wavefield, whereas the superimposed small-scale fluctuations are inferred from the associated reflected component. An important and distinguishing feature of our methodology is that, in contrast to previous related approaches (e.g., Schmelzbach et al. 2012; Liu et al. 2018; Xu et al. 2021), it does not require any borehole calibration and/or conditioning information. It does, however, inherently rely upon the presence of diffractions in the GPR data. In this regard, it is important to note that, although diffractions are often not immediately obvious in a GPR profile, they can become much more evident after wavefield separation. This is clearly illustrated in Figure 8.

The proposed technique was tested and validated on synthetic data corresponding to two velocity models of differing complexity and realism: one an idealized layered model containing a small number of discrete diffractors, and the other a stochastic facies-based model emulating the typical heterogeneity observed in surficial alluvial environments (e.g., Gelhar 1993; Tronicke et al. 2004; Tronicke and Holliger 2005). These synthetic tests not only illustrate the fundamental validity and robustness of our method, but also allow us to identify a number of features that merit attention during its application. Successful validation of our approach on the BHRS field data further illustrates its capacity for estimating complex velocity structures.

Results for our synthetic test involving the stochastic subsurface model (Figures 4 and 5) showed a loss of accuracy in the shallowest part of the inferred velocity distribution due to the elimination of the direct air and ground arrivals, which removed important reflections from this zone. Processing techniques used for this purpose, such as subtracting the average trace in a corresponding time window, will thus affect the inferred velocity model over an initial depth range of roughly 1-2 dominant wavelengths (Figures 4 and 5). Another interesting feature emerging from the stochastic synthetic example is the fact that we fail to fully resolve the thin low-velocity zone between ~2 m and ~3.5 m depth, notably in the central and right-hand side of the profile. A bias in the estimated background velocity distribution over these depths (Figure 5d) is likely the cause of this result. Given that this region has a density of diffractions that is comparable to the rest of the model, this may point to the inherently limited resolution of the inferred background velocity field. Under ideal circumstances, diffraction-based velocity analysis can be expected to achieve a resolution on the order of one dominant wavelength, which for the considered synthetic data is of the order of ~1 m. In practice, however, the achievable resolution critically depends on the so-called smoothing radius parameter, which controls the regularization of a number of steps in the diffraction velocity analysis procedure (Fomel et al., 2007). As recently illustrated by Yuan et al. (2019), a smoothing radius that is too small leads to unstable estimates of the diffraction-derived velocity model, whereas one that is too large will lower unnecessarily its resolution. While we made every effort to determine an optimal value of the smoothing radius for all data considered in this study, there may be regions in the final velocity model where the large- and small-scale components inadequately complement each other due to the limited resolution of the former.

Arguably, the most important criterion that must be fulfilled for our method to perform satisfactorily is the presence of an ample amount evenly distributed diffractions throughout the recorded constant-offset GPR section. Given the inherent heterogeneity of the shallow subsurface (e.g., Gelhar, 1993; Hubbard and Rubin, 2005; Dafflon et al., 2009; Xu et al., 2021), this condition is likely to be fulfilled even if the diffracted energy is not directly obvious in the original recorded data (Figures 5 and 8). Nonetheless, in the case where an sufficient amount of diffracted energy cannot be retrieved through wavefield separation and/or where the diffraction events are highly unevenly distributed throughout the probed subsurface region, standard common-midpoint-type analyses may still be used to estimate the large-scale velocity structure with our methodology. Under these circumstances, only the estimation of the background field would change, and the inversion for the small-scale velocity fluctuations would remain the same.

Two final assumptions upon which our method relies are that the recorded GPR wavefield is largely non-dispersive and is dominated by single scattering. This allows us to use a convolutional model to describe the reflection data, which in turn permits us to pose the velocity perturbation estimation procedure as a highly efficient linear inverse problem. Limited signal attenuation, and thus limited dispersion, is a prerequisite for acquiring surface-based common-offset GPR reflection data of adequate quality and depth of penetration. The practical validity of this assumption is notably underscored by the success of numerous studies explicitly relying upon an adequate estimation of the GPR source wavelet (e.g., Schmelzbach et al., 2012; Schmelzbach and Huber, 2015; Liu et al., 2018; Xu et al., 2021). While it is theoretically conceivable that there exist environments where multiple scattering becomes sufficiently important in GPR studies, the results of extensive testing of the convolutional model on synthetic and field data suggest that the effects of multiples are largely negligible in near-surface environments (e.g., Irving et al., 2009; Schmelzbach et al., 2012; Xu et al., 2020,2021). Indeed, in such environments, the combination of small reflection coefficients and signal attenuation due to conductivity-related losses means that multiply reflected energy is not strong. The latter is consistent with a methodological study involving acoustic waves in strongly heterogeneous environments, where it was found that multiple scattering only becomes important for strong local velocity fluctuations, corresponding to standard deviations of the order of 10% and more, in combination with long propagation paths in excess of ~20 dominant wavelengths (e.g., Holliger, 1997). These conditions are generally not fulfilled for surface-based constant-offset GPR reflection data.

An important characteristic of this work is that the proposed methodology is rather straightforward. After basic processing of the GPR data in MATLAB, wavefield separation, diffraction velocity analysis, and Dix inversion are carried out using the Madagascar software package, which is well-established for this purpose. The subsequent wavelet estimation and L1-norm inversion are then again performed in MATLAB. For all of the datasets considered in this study, the total time required to complete all of the steps in our workflow is on the order of one day. The IRLS inversion procedure itself proved to be stable and to converge to consistent estimates of the velocity perturbation field after approximately five iterations. In practical terms, the latter amounted to less than one minute of CPU time on a modest laptop computer. Finally, the inherent computational efficiency of the convolutional model used in our approach implies that the extension of the proposed method to 3D is conceptually straightforward. The only challenge that we anticipate in this regard is the still somewhat limited practical maturity of 3D diffraction velocity analysis techniques (e.g., Merzlikin et al. 2017; Bauer et al., 2020). A direct benefit of 3D analysis is that errors introduced into the background velocity estimation procedure by out-of-plane diffractions can be avoided.

Acknowledgements

Yu Liu gratefully acknowledges financial support of this work through the China Scholarship Council (CSC grant number 201806320359). The considered GPR field data were collected by Michael Knoll and Warren Barrash as part of the initial BHRS characterization, and were kindly provided to us by John Bradford together with the corresponding neutron-neutron porosity logs.

Data availability

The data underlying this article will be shared on reasonable request to the corresponding author.

References

Annan, A.P., 2005. Ground-penetrating radar, in Near-surface geophysics, pp. 357–438, Society of Exploration Geophysicists. doi:10.1190/1.9781560801719.ch11

Barrash, W. & Clemo, T., 2002. Hierarchical geostatistics and multifacies systems: Boise Hydrogeophysical Research Site, Boise, Idaho, Water Resour. Res., 38(10), 1-18. doi:10.1029/2002wr001436

Bauer, A., Schwarz, B. & Gajewski, D., 2020. Velocity inversion and scatterer detection with 3D P-cable data, in SEG Technical Program Expanded Abstracts 2020, pp. 3644-3648,

Society of Exploration Geophysicists. doi: 10.1190/segam2020-3426557.1
Bradford, J.H., 2008. Measuring water content heterogeneity using multifold GPR with reflection tomography, Vadose Zone J., 7, 184–193. doi:10.2136/vzj2006.0160
Bradford, J.H., Clement, W.P. & Barrash, W., 2009. Estimating porosity with ground-penetrating radar reflection tomography: A controlled 3-D experiment at the Boise Hydrogeophysical Research Site. Water Resour. Res., 45(4). doi:10.1029/2008WR006960
Busch, S., van der Kruk, J., Bikowski, J. & Vereecken, H., 2012. Quantitative conductivity and permittivity estimation using full-waveform inversion of on-ground GPR data, Geophysics, 77(6), H79-H91. doi:10.1190/geo2012-0045.1
Buttkus, B., 2000. Spectral analysis and filter theory in applied geophysics, pp.521-524, Springer Science & Business Media. doi:10.1007/978-3-642-57016-2
Claerbout, J.F. & Muir, F., 1973. Robust modeling with erratic data, Geophysics, 38(5), 826–844. doi:10.1190/1.1440378
Clair, J.S. & Steven Holbrook, W., 2017. Measuring snow water equivalent from common-offset GPR records through migration velocity analysis, Cryosphere, 11, 2997–3009. doi:10.5194/tc-11-2997-2017
Dafflon, B., Irving, J. & Barrash, W., 2011. Inversion of multiple intersecting high-resolution crosshole GPR profiles for hydrological characterization at the Boise Hydrogeophysical Research Site, J. Appl. Geophys., 73(4), 305–314. doi:10.1016/j.jappgeo.2011.02.001
Dafflon, B., Irving, J. & Holliger, K., 2009. Use of high-resolution geophysical data to characterize heterogeneous aquifers: Influence of data integration method on hydrological predictions, Water Resour. Res., 45(9), 1–12. doi:10.1029/2008WR007646
Decker, L., Merzlikin, D. & Fomel, S., 2017. Diffraction imaging and time-migration velocity analysis using oriented velocity continuation, Geophysics, 82(2), U25–U35. doi:10.1190/GEO2016-0141.1
Ekblom, H., 1973. Calculation of linear best L_p-approximation, BIT Numerical Mathematics, 13(3), 292–300.
Ernst, J.R., Green, A.G., Maurer, H. & Holliger, K., 2007. Application of a new 2D time-domain full-waveform inversion scheme to crosshole radar data, Geophysics, 72(5), J53-J64. doi:10.1190/1.2761848
Farquharson, C.G. & Oldenburg, D.W., 1998. Non-linear inversion using general measures of data misfit and model structure, Geophys. J. Int., 134, 213–227. doi:10.1046/j.1365-246x.1998.00555.x
Fomel, S., 2002. Applications of plane-wave destruction filters, Geophysics, 67(6), 1946–1960. doi:10.1190/1.1527095
Fomel, S., 2003. Time-migration velocity analysis by velocity continuation, Geophysics, 68(5), 1662–1672. doi:10.1190/1.1620640
Fomel, S., 2007a. Shaping regularization in geophysical-estimation problems. *Geophysics*, 72(2), R29-R36. doi:10.1190/1.2433716
Fomel, S., 2007b. Local seismic attributes, Geophysics, 72(3), A29-A33. doi:10.1190/1.2437573
Fomel, S., 2009. Velocity analysis using AB semblance, Geophys. Prospect., 57(3), 311–321. doi:10.1111/j.1365-2478.2008.00741.x
Fomel, S. & Guitton, A., 2006. Regularizing seismic inverse problems by model

reparameterization using plane-wave construction, Geophysics, 71(5), A43–A47. doi:10.1190/1.2335609
Fomel, S., Landa, E. & Taner, M.T., 2007. Poststack velocity analysis by separation and imaging of seismic diffractions, Geophysics, 72(6), U89-U94. doi:10.1190/1.2781533
Forte, E., Dossi, M., Colucci, R.R. & Pipan, M., 2013. A new fast methodology to estimate the density of frozen materials by means of common offset GPR data, J. Appl. Geophys., 99, 135–145. doi:10.1016/j.jappgeo.2013.08.013
Forte, E., Dossi, M., Pipan, M. & Colucci, R.R., 2014. Velocity analysis from common offset GPR data inversion: Theory and application to synthetic and real data, Geophys. J. Int., 197(3), 1471–1483. doi:10.1093/gji/ggu103
Gelhar, L.W., 1993. Stochastic subsurface hydrology, pp.390. Prentice-Hall.
Gibson, B.S. & Levander, A.R., 1990. Apparent layering in common-midpoint stacked images of two-dimensionally heterogeneous targets, Geophysics, 55(11), 1466–1477. doi:10.1190/1.1442794
Greaves, R.J., Lesmes, D.P., Lee, J.M. & Toksöz, M.N., 1996. Velocity variations and water content estimated from multi-offset, ground-penetrating radar, Geophysics, 61(3), 683–695. doi:10.1190/1.1443996
Hochstetler, D.L., Barrash, W., Leven, C., Cardiff, M., Chidichimo, F. & Kitanidis, P.K., 2016. Hydraulic tomography: Continuity and discontinuity of high-K and low-K zones. Groundwater, 54(2), 171–185. doi:10.1111/gwat.12344
Holliger, K., 1997. Seismic scattering in the upper crystalline crust based on evidence from sonic logs, Geophys. J. Int., 128, 65–72. doi:10.1111/j.1365-246X.1997.tb04071.x
Holliger, Klaus, Levander, A., Carbonell, R. & Hobbs, R., 1994. Some attributes of wavefields scattered from Ivrea-type lower crust, Tectonophysics, 232, 267–279. doi:10.1016/0040-1951(94)90089-2
Hubbard, S.S. & Rubin, Y. (2005) Introduction to hydrogeophysics, in Hydrogeophysics, pp. 3–21, Springer. doi:10.1007/1-4020-3102-5
Huisman, J.A., Hubbard, S.S., Redman, J.D. & Annan, A.P., 2003. Measuring soil water content with ground penetrating radar: A review, Vadose Zone J., 2(4), 476–491. doi:10.2136/vzj2003.4760
Irving, J. & Knight, R., 2006. Numerical modeling of ground-penetrating radar in 2-D using MATLAB, Comput. Geosci., 32(9), 1247–1258. doi:10.1016/j.cageo.2005.11.006
Irving, J., Knight, R. & Holliger, K., 2009. Estimation of the lateral correlation structure of subsurface water content from surface-based ground-penetrating radar reflection images, Water Resour. Res., 45(12). doi:10.1029/2008WR007471
Klotzsche, A., Jonard, F., Looms, M.C., Kruk, J. van der & Huisman, J.A., 2018. Measuring soil water content with ground penetrating radar: A decade of progress, Vadose Zo. J., 17(1), 1–9. doi:10.2136/vzj2018.03.0052
Klotzsche, A., Vereecken, H. & Kruk, J. van der., 2019. Review of crosshole ground-penetrating radar full-waveform inversion of experimental data: Recent developments, challenges, and pitfalls, Geophysics, 84(6), H13–H28. doi:10.1190/geo2018-0597.1
Knight, R., 2001. Ground penetrating radar for environmental applications, Annu. Rev. Earth Planet. Sci., 29, 229–255. doi:10.1146/annurev.earth.29.1.229
Lai, W.W.-L., Derobert, X. & Annan, P., 2018. A review of Ground Penetrating Radar

application in civil engineering: A 30-year journey from Locating and Testing to Imaging and Diagnosis, NDT&E international, 96, 58–78. doi:10.1016/j.ndteint.2017.04.002

Lampe, B. & Holliger, K., 2003. Effects of fractal fluctuations in topographic relief, permittivity and conductivity on ground-penetrating radar antenna radiation, Geophysics, 68(6), 1934–1944. doi:10.1190/1.1635047

Lavoué, F., Brossier, R., Métivier, L., Garambois, S. & Virieux, J., 2014. Two-dimensional permittivity and conductivity imaging by full waveform inversion of multioffset GPR data: A frequency-domain quasi-Newton approach, Geophys. J. Int., 197(1), 248–268. doi:10.1093/gji/ggt528

Liu, Y., Shi, Z., Wang, B. & Yu, T., 2018. GPR impedance inversion for imaging and characterization of buried archaeological remains: A case study at Mudu city cite in Suzhou, China, J. Appl. Geophys., 148, 226–233. doi:10.1016/j.jappgeo.2017.12.002

Merzlikin, D., Meckel, T.A., Fomel, S. & Sripanich, Y., 2017. Diffraction imaging of high-resolution 3D P-cable data from the Gulf of Mexico using azimuthal plane-wave destruction, First Break, 35(2). doi:10.3997/1365-2397.2017002

Novais, A., Costa, J. & Schleicher, J., 2008. GPR velocity determination by image-wave remigration, J. Appl. Geophys., 65, 65–72. doi:10.1016/j.jappgeo.2008.05.001

Oldenburg, D.W., Scheuer, T. & Levy, S., 1983. Recovery of the acoustic impedance from reflection seismograms, Geophysics, 48(10), 1318–1337. doi:10.1190/1.1441413

Perroud, H. & Tygel, M., 2005. Velocity estimation by the common-reflection-surface (CRS) method: Using ground-penetrating radar data, Geophysics, 70(6), B43-B52. doi:10.1190/1.2106047

Poppeliers, C., 2007. Estimating vertical stochastic scale parameters from seismic reflection data: Deconvolution with non-white reflectivity, Geophys. J. Int., 168(2), 769–778. doi:10.1111/j.1365-246X.2006.03239.x

Pullammanappallil, S., Levander, A. & Larkin, S.P., 1997. Estimation of crustal stochastic parameters from seismic exploration data, J. Geophys. Res.- Solid Earth, 102(B7), 15269–15286. doi:10.1029/97JB01144

Schmelzbach, C., Tronicke, J. & Dietrich, P., 2012. High-resolution water content estimation from surface-based ground-penetrating radar reflection data by impedance inversion, Water Resour. Res., 48(8). doi:10.1029/2012WR011955

Schmelzbach, C. & Huber, E., 2015. Efficient deconvolution of ground-penetrating radar data, IEEE Trans. Geosci. Remote Sens., 53(9), 5209–5217. doi:10.1109/TGRS.2015.2419235

Scholer, M., Irving, J. & Holliger, K., 2010. Estimation of the correlation structure of crustal velocity heterogeneity from seismic reflection data, Geophys. J. Int., 183(3), 1408–1428. doi:10.1111/j.1365-246X.2010.04793.x

Thiran, J.P., 1971. Recursive digital filters with maximally flat group delay, IEEE Trans. Circuit Theory, 18, 659–664. doi:10.1109/TCT.1971.1083363

Tronicke, J. & Holliger, K., 2005. Quantitative integration of hydrogeophysical data: Conditional geostatistical simulation for characterizing heterogeneous alluvial aquifers, Geophysics, 70(3), H1–H10. doi:10.1190/1.1925744

Tronicke, J., Holliger, K., Barrash, W. & Knoll, M.D., 2004. Multivariate analysis of cross-hole georadar velocity and attenuation tomograms for aquifer zonation, Water Resour. Res., 40(1). doi:10.1029/2003WR002031

Velis, D.R., 2008. Stochastic sparse-spike deconvolution, Geophysics, 73(1), R1–R9. doi:10.1190/1.2790584
Warren, C., Giannopoulos, A. & Giannakis, I., 2016. gprMax: Open source software to simulate electromagnetic wave propagation for Ground Penetrating Radar, Comput. Phys. Commun., 209, 163–170. doi:10.1016/j.cpc.2016.08.020
Xu, Z., Irving, J., Lindsay, K., Bradford, J., Zhu, P. & Holliger, K., 2020. Estimation of the 3D correlation structure of an alluvial aquifer from surface-based multi-frequency ground-penetrating radar reflection data, Geophys. Prospect., 68(2), 678–689. doi:10.1111/1365-2478.12857
Xu, Z., Irving, J., Liu, Y., Zhu, P. & Holliger, K., 2021. Conditional stochastic inversion of common-offset GPR reflection data, Geophysics. doi:10.1190/geo2020-0639.1
Yilmaz, Ö., 2001. Seismic data analysis: Processing, inversion, and interpretation of seismic data, Society of exploration geophysicists.
Yuan, H., Montazeri, M., Looms, M.C. & Nielsen, L., 2019. Diffraction imaging of ground-penetrating radar data. Geophysics, 84(3), H1–H12. doi:10.1190/geo2018-0269.1
Zeng, Z., Chen, X., Li, J., Chen, L., Lu, Q. & Liu, F., 2015. Recursive impedance inversion of ground-penetrating radar data in stochastic media, Appl. Geophys., 12(4), 615–625. doi:10.1007/s11770-015-0514-0

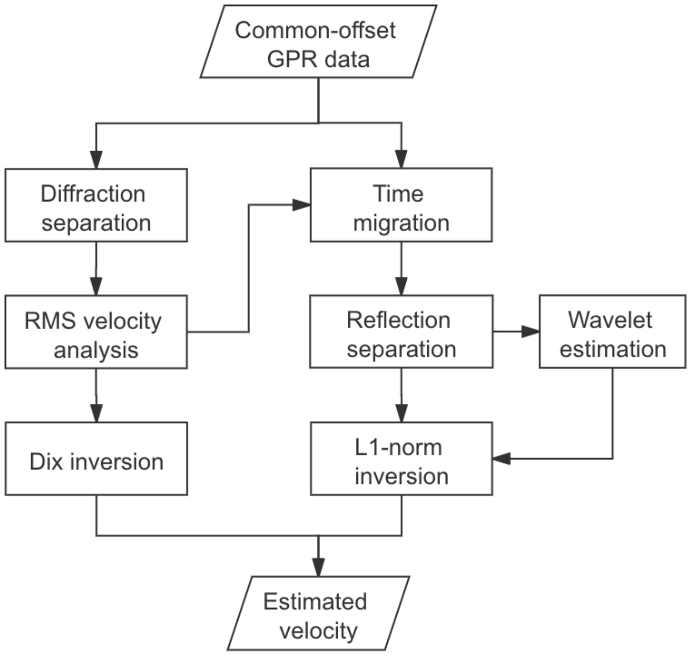

Figure 1. Flowchart illustrating the proposed method for estimating the detailed subsurface velocity structure from surface-based common-offset GPR reflection data.

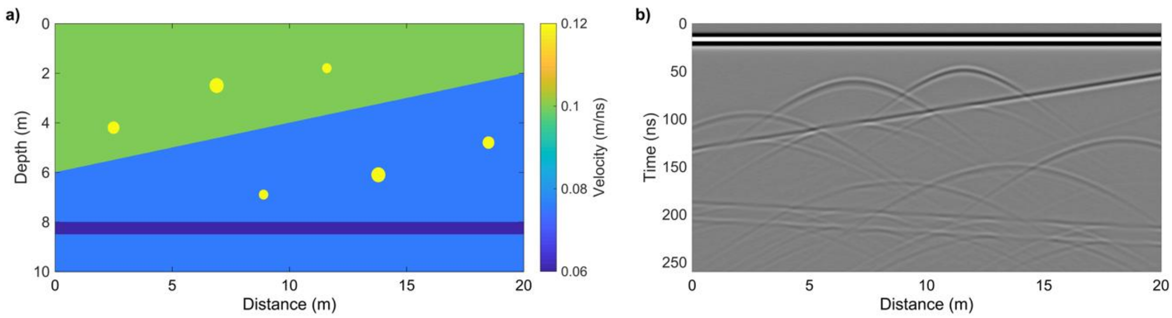

Figure 2. a) Layered model velocity with discrete diffractors and **b)** corresponding synthetic common-offset GPR reflection data with 2% Gaussian random noise added.

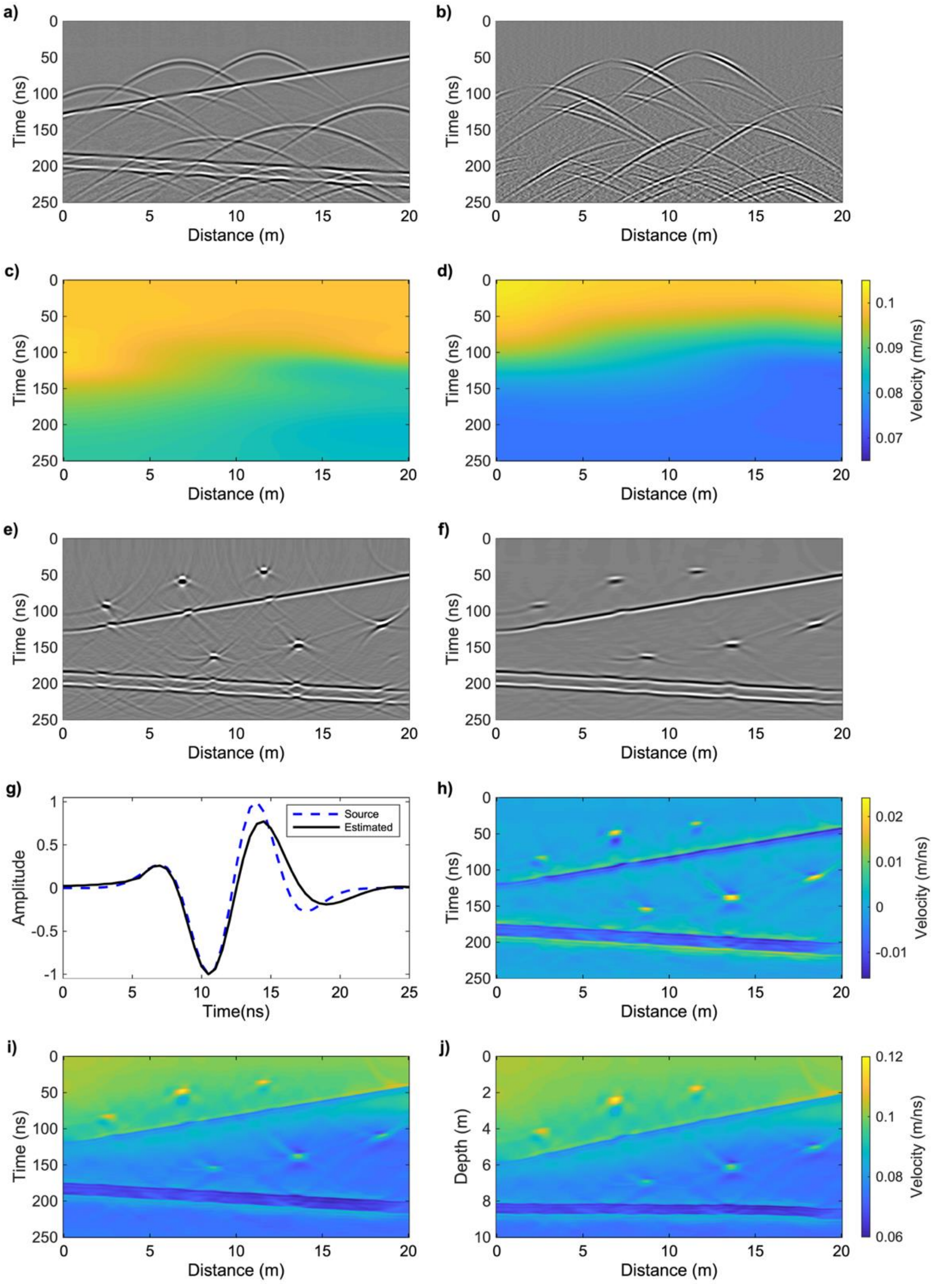

Figure 3. Velocity estimation process for the layered synthetic velocity model presented in Figure 2a. From the **a)** processed GPR section, the **b)** diffracted wavefield is separated and used to estimate the **c)** RMS velocity structure. Using Dix inversion, the **d)** low-frequency background velocity field $v_0(x, t)$ is obtained. **e)** Time-migrated GPR section based on the RMS velocity structure, from which the **f)** reflected wavefield is obtained. **g)** Comparison of estimated GPR wavelet with the true source wavelet. **h)** Velocity perturbation field $\Delta v(x, t)$ obtained by inverting the reflected wavefield. The final estimated velocity structure (background+perturbation) is shown in terms of **i)** traveltime and **j)** depth.

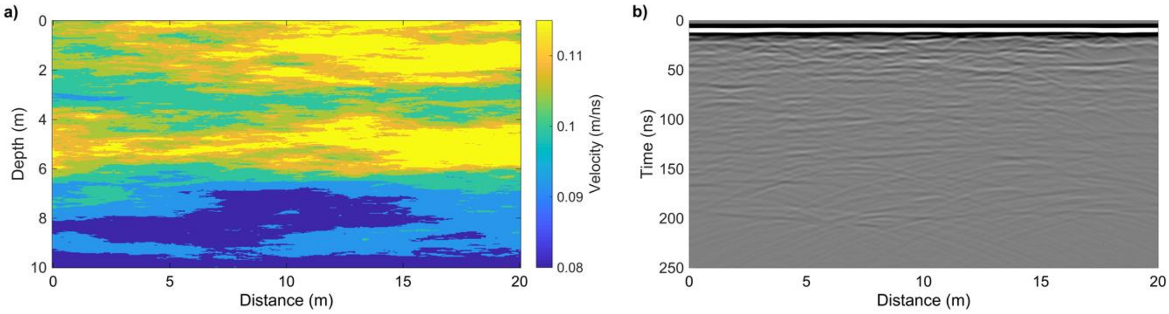

Figure 4. a) Stochastic velocity model and **b)** corresponding synthetic common-offset GPR reflection data with 2% Gaussian random noise added.

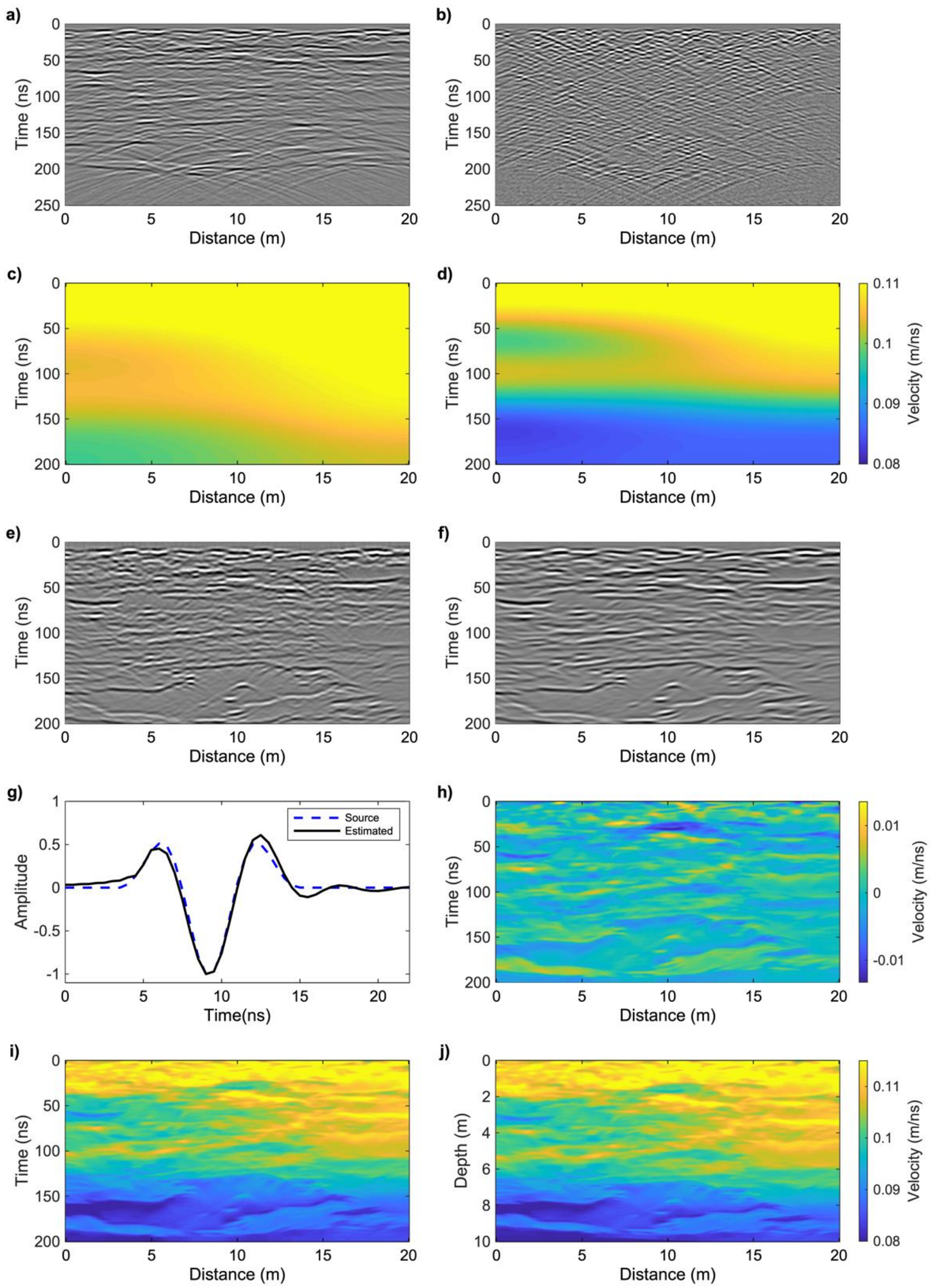

Figure 5. Velocity estimation process for the stochastic synthetic velocity model presented in Figure 4a. From the **a)** processed GPR section, the **b)** diffracted wavefield is separated and used to estimate the **c)** RMS velocity structure. Using Dix inversion, the **d)** low-frequency background velocity field $v_0(x, t)$ is obtained. **e)** Time-migrated GPR section based on the RMS velocity structure, from which the **f)** reflected wavefield is obtained. **g)** Comparison of estimated GPR wavelet with the true source wavelet. **h)** Velocity perturbation field $\Delta v(x, t)$ obtained by inverting the reflected wavefield. The final estimated velocity structure (background+perturbation) is shown in terms of **i)** traveltime and **j)** depth.

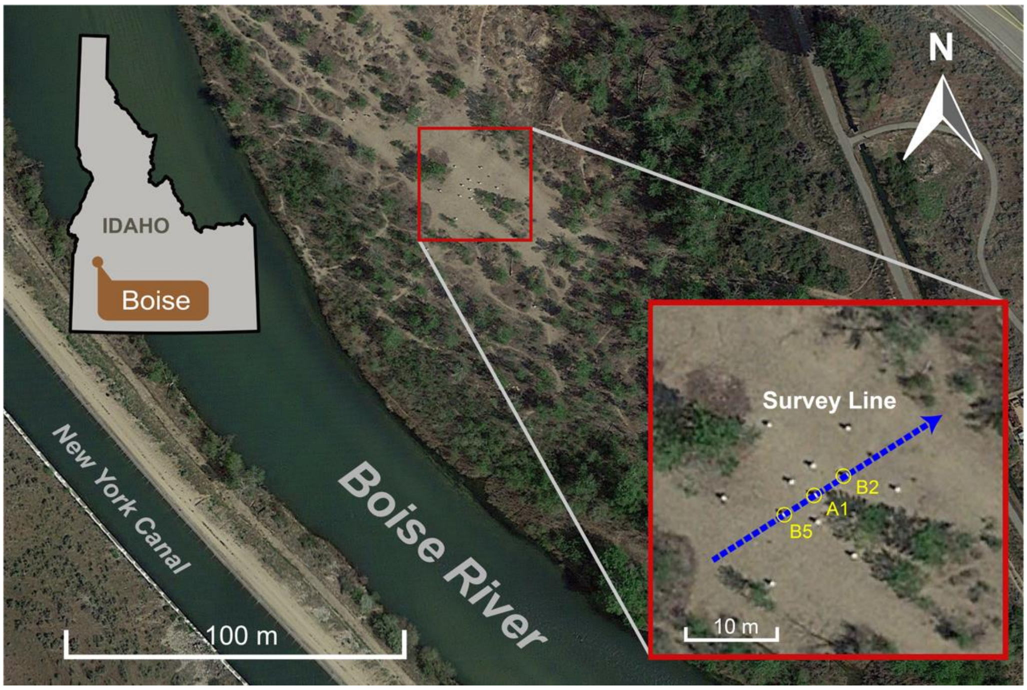

Figure 6. Map of the BHRS showing the location of considered common-offset GPR reflection profile (blue dashed line). The profile is aligned with boreholes B5, A1, and B2 (yellow circles).

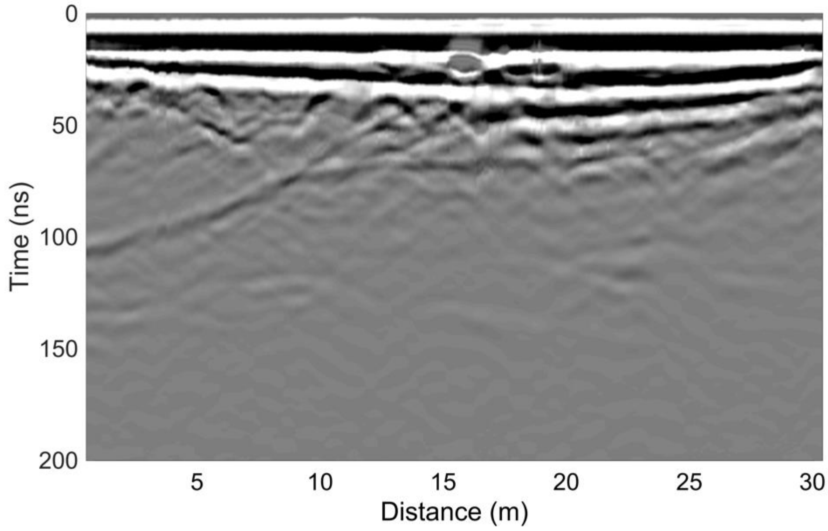

Figure 7. Common-offset GPR reflection section from the BHRS after minor preprocessing consisting of time-zero correction and “de-wow” filtering.

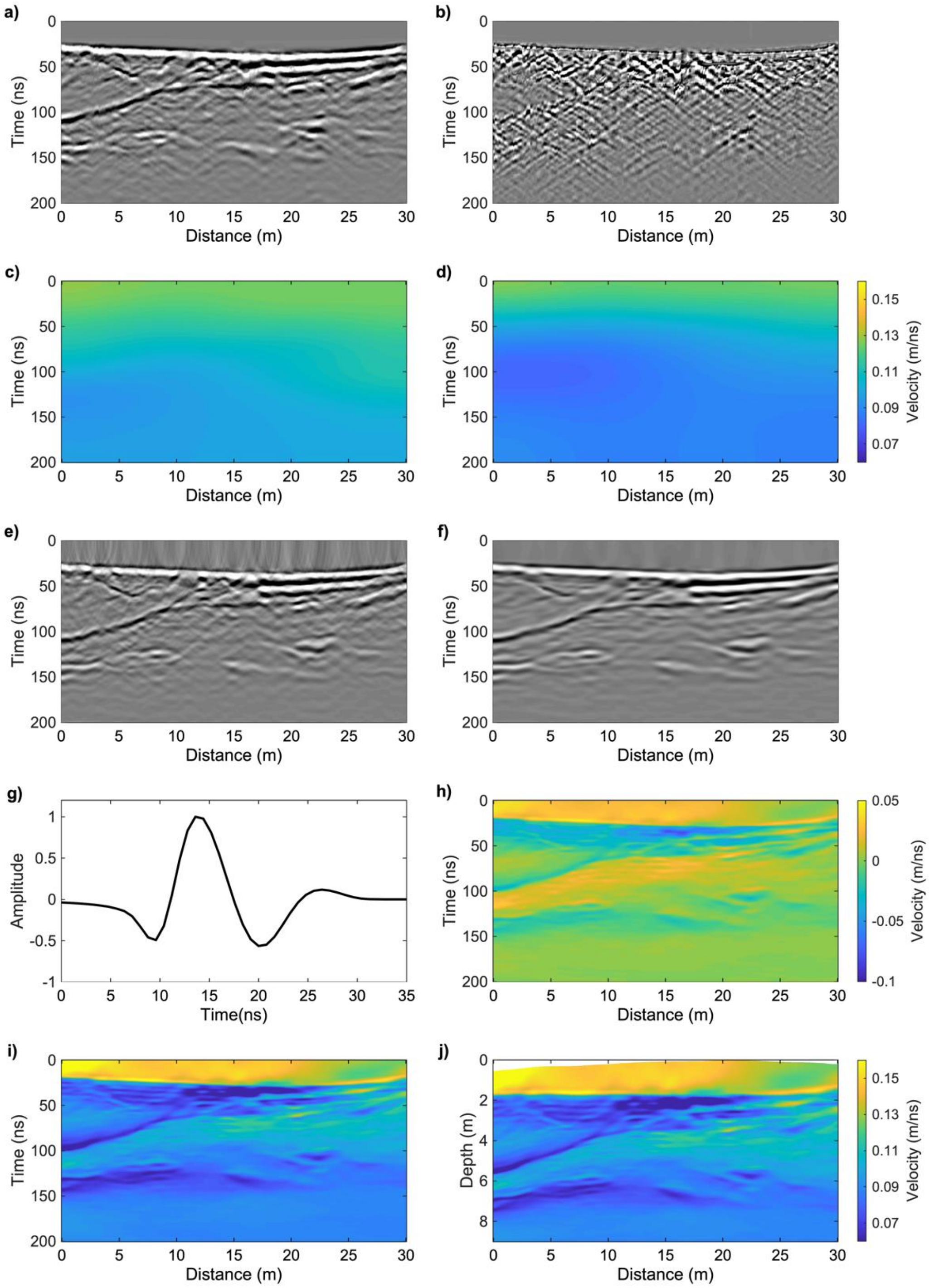

Figure 8. Velocity estimation process for the BHRS field data presented in Figure 7. From the **a)** processed GPR section, the **b)** diffracted wavefield is separated and used to estimate the **c)** RMS velocity structure. Using Dix inversion, the **d)** low-frequency background velocity field $v_0(x,t)$ is obtained. **e)** Time-migrated GPR section based on the RMS velocity structure, from which the **f)** reflected wavefield is obtained. **g)** Estimated GPR source wavelet. **h)** Velocity perturbation field $\Delta v(x,t)$ obtained by inverting the reflected wavefield. The final estimated velocity structure (background+perturbation) is shown in terms of **i)** traveltime and **j)** depth.

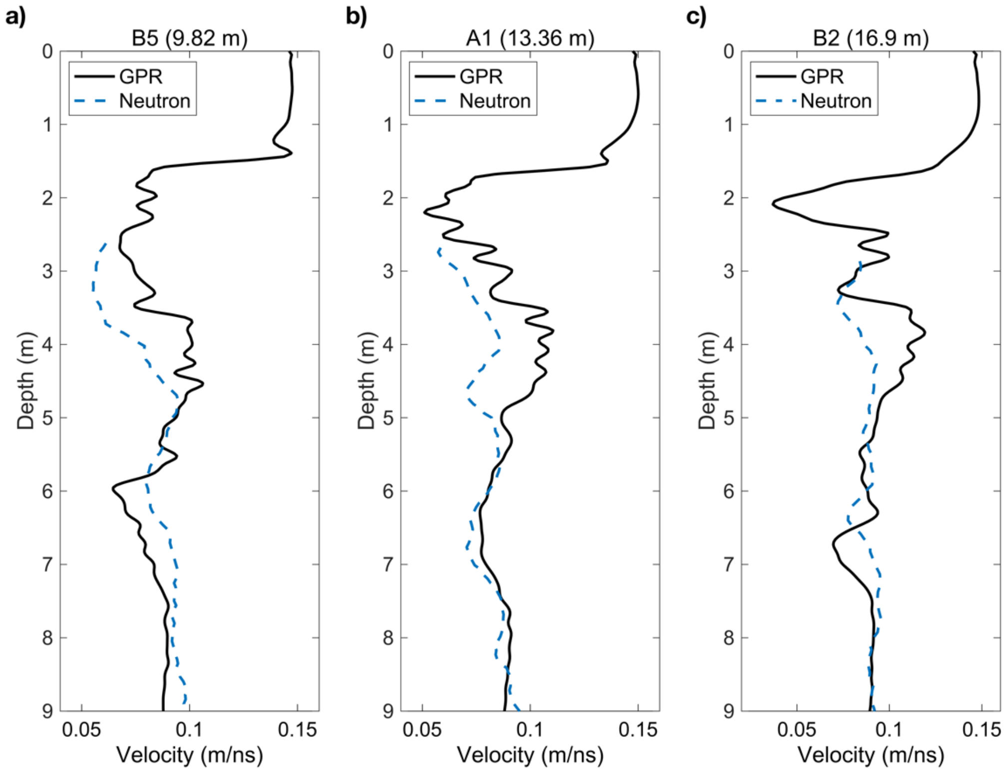

Figure 9. Comparison of the velocity estimated from the common-offset GPR reflection data from the BHRS along boreholes **a)** B5, **b)** A1 and **c)** B2 (black solid lines) with the corresponding converted neutron-neutron porosity logs (blue dashed lines).